Chapter 19
High-energy Emission from the Polar Cap and Slot Gap

Alice K. Harding

19.1 Introduction

Forty years after the discovery of rotation-powered pulsars, we still do not understand many aspects of their pulsed emission. In the last few years there have been some fundamental developments in acceleration and emission models. In this Chapter I will review both the basic physics of the models as well as the latest developments in understanding the high-energy emission of rotation-powered pulsars, with particular emphasis on the polar-cap and slot-gap models. Special and general relativistic effects play important roles in pulsar emission, from inertial frame-dragging near the stellar surface to aberration, time-of-flight and retardation of the magnetic field near the light cylinder. Understanding how these effects determine what we observe at different wavelengths is critical to unraveling the emission physics.

Rotation-powered pulsars are fascinating astrophysical sources and excellent laboratories for study of fundamental physics of strong gravity, strong magnetic fields, high densities and relativity. The major advantage we have in studying pulsars is that we know they are rotating neutron stars and that they derive their power from rotational energy loss. The challenge is then to understand how they convert this source of power into the visible radiation. It is generally agreed that this occurs through acceleration of charged particles to extremely relativistic energies, using the rotating magnetic field as a unipolar inductor to create very high electric potentials. Beyond this fundamental, there is a large divergence of thought on what comes next: whether the acceleration occurs in the strong field near the neutron star surface or in the outer magnetosphere near the speed of light cylinder, or even beyond the light cylinder in the wind zone. The particle acceleration may well be occurring in all of these regions, either in the same pulsar or in pulsars of different ages.

A.K. Harding
Astrophysics Science Division, NASA Goddard Space Flight Center
e-mail: harding@twinkie.gsfc.nasa.gov

In recent years, there has been much activity both in new detections and in theoretical study of rotation-powered pulsars. Multibeam radio surveys at the Parkes Telescope [23, 50] have increased the population of known radio pulsars to more than 1,700. In addition, extended radio observations of supernova remnants and unidentified γ-ray sources have discovered a number of young pulsars that are too radio-faint to be detected by surveys [12]. Although pulsed emission at other wavelengths has been detected from only a small fraction of these, this number is growing as well. At the present time, there are seven pulsars with high-confidence detection of γ-ray pulsations (cf. Chap. 23), about 30 having X-ray pulsations [42] and 10 with optical pulsations [52].

This Chapter will review both the fundamental physics and latest theoretical developments of acceleration and radiation in polar cap models. The complementary Chap. 18 reviews acceleration and radiation in the outer gap model.

19.2 Acceleration Near the Polar Cap and Beyond

A magnetic dipole rotating in vacuum will induce an electric field both along and across the magnetic field lines [18]. In the case of a pulsar, with high angular velocity Ω and surface dipole fields $B_0 \sim 10^{12}$ G, the electric force parallel to the magnetic field just above the neutron star surface exceeds the gravitational force by many orders of magnitude. Vacuum conditions therefore cannot exist outside a pulsar, since charges can be pulled from the stellar surface [24]. If the charge density reaches the Goldreich-Julian value,

$$\rho_{GJ} = \frac{\nabla \cdot \mathbf{E}}{4\pi} \approx -\frac{\Omega \cdot \mathbf{B}}{2\pi c}, \tag{19.1}$$

derived from the condition

$$\mathbf{E} = -\frac{(\Omega \times r) \times \mathbf{B}}{c}, \tag{19.2}$$

then the electric field parallel to the magnetic field vanishes. This is the force-free solution where charges and magnetic field co-rotate with the star. Corotation must break down near the light cylinder, $R_L = \Omega/c$, due to particle inertia. But if vacuum cannot surround a pulsar, neither can a completely force-free magnetosphere, since in that case no acceleration of charge, currents or radiation would exist. A real pulsar must operate somewhere between the two extremes of the vacuum and the force-free states, but a self-consistent, global solution has not yet been found. Global magnetospheric simulations study how a rotating neutron star magnetosphere fills with charge from the vacuum state. The resulting domes and torii of charge that build up near the pole and equator [44, 60] seem to be unstable [67], but the particle-in-cell codes cannot run long enough to reach a stable magnetospheric configuration. However, it seems that a near force-free magnetosphere [68] cannot result only from charges flowing out of the stellar surface, but requires some extra source of charge created in the magnetosphere above the surface. This extra source of charge

is thought to be production of electron-positron pairs by the photons radiated by accelerating particles. The pulsar magnetosphere must somehow be made up of self-consistent force-free and non-force-free regions in balance with each other. One way to determine the structure of these regions is to study the microphysics of the electrodynamics and charge flow at different sites where acceleration may occur. One of these sites, the polar cap accelerator, is near the neutron star surface on the open field lines that cross the light cylinder.

19.2.1 Polar Cap Accelerators

The two main types of polar cap accelerator are vacuum gaps [64, 72] and space-charge limited flow (SCLF) gaps [6, 33]. There are binding (or cohesive) forces on charged particles in the neutron star surface due to the lattice structure in a strong magnetic field, such that particles are free only if the surface layers are above the thermionic emission temperature. For electrons, this temperature is [72]

$$T_e \cong 3.6 \times 10^5 K \left(\frac{Z}{26}\right)^{0.8} \left(\frac{B_0}{10^{12}G}\right)^{0.4} \tag{19.3}$$

and for ions it is

$$T_i \cong 3.5 \times 10^5 K \left(\frac{B_0}{10^{12}G}\right)^{0.73} \tag{19.4}$$

where B_0 is the surface magnetic field strength and Z is the atomic number of matter in the surface layer. If the surface temperature, $T_s < T_{i,e}$, then charges are trapped in the surface and the full vacuum electric field, $E_\parallel = \Omega B_0 R$, where R is the neutron star radius, exists above the surface. If $T_s > T_{i,e}$, then charges are "boiled off" the surface layers and can flow along the open field lines in SCLF. Measured surface temperatures of pulsars are typically $T_s > 0.5 - 3.0 \times 10^6$ K, above T_e and T_i for the normal range $B_0 \lesssim 10^{13}$ of surface fields. However, a few high-field pulsars or magnetars may have $T_s < T_{i,e}$ and vacuum gaps [72, 76]. If $T_s > T_{i,e}$ and the full Goldreich-Julian charge can be supplied right about the surface, the true charge density along each field line will drop faster, $\rho \propto r^{-3}$, than ρ_{GJ} as the dipole field lines flare. A SCLF electric field, $\nabla \cdot E_\parallel = (\rho - \rho_{GJ})/\varepsilon_0$ grows with altitude. The two types of accelerator thus differ by the surface boundary condition: where $\rho(R) = 0$, $E_\parallel(R) \neq 0$ for vacuum gaps and $\rho(R) = \rho_{GJ}$, $E_\parallel(R) = 0$ for SCLF accelerators. The form of $E_\parallel$ in SCLF accelerators is thus sensitive to the detailed distribution of the charge density, which depends both on the open field line geometry as well as the compactness of the neutron star. At altitudes $\{z \ll \theta_{PC}, z \gg \theta_{PC}\}$, with $z \equiv (r/R - 1)$ being the height above the surface,

$$E_\parallel \simeq B_0 \theta_{PC}^2 \left[\{z, \theta_{PC}^2 \left(\tfrac{r}{R}\right)^{-4}\} \kappa \cos\alpha + \{z, \theta_{PC}^2 \left(\tfrac{r}{R}\right)^{-1/2}\} \tfrac{\theta_{PC}}{2} \sin\alpha \cos\varphi \right]$$
$$\times [1 - \left(\tfrac{\theta}{\theta_{PC}}\right)^2] \tag{19.5}$$

[33, 59], where θ and φ are the magnetic polar and azimuth angles, α is the magnetic inclination angle to the rotation axis, $\kappa = 2GI/(c^2 R^3)$ is the stellar compactness parameter, $\theta_{PC} \simeq (\Omega R/c)^{1/2}$ is the polar cap half-angle and I the neutron star moment of inertia. The first term in (19.5) is due to inertial frame dragging near the neutron star surface, and dominates for small r and low inclination, while the second term is due to the flaring of the field lines.

Both accelerators will be self-limited by the development of pair cascades, at altitudes where the particles reach high enough Lorentz factors to radiate γ-ray photons. The dominant process in most pulsars is one-photon pair production, which can occur only in very strong magnetic (or electric) fields. In this process, the magnetic field absorbs the extra momentum of a photon having the energy required to create a pair, so that the threshold condition on the photon energy is $\varepsilon_\gamma = 2mc^2/\sin\theta_{\gamma B}$, where $\theta_{\gamma B}$ is the angle between the photon propagation direction and the local magnetic field. The accelerated particles moving along magnetic field lines with high Lorentz factors radiate γ-ray photons at very small angles to the field ($\theta_0 \sim 1/\gamma$), so the one-photon pair production rate for these photons is initially zero. However, as they propagate through the curved dipole field, their angle increases until the threshold condition and the attenuation coefficient becomes large. The voltage across a vacuum gap breaks down when a stray γ-ray crosses the magnetic field within the gap and creates a pair. The electron accelerates upward/downward for $\Omega \cdot B(>,<)0$ over the polar cap, and the positron accelerates in the opposite direction as shown in Fig. 19.1. Both particles produce more pairs when their radiated photons reach the pair threshold, causing a pair avalanche and sudden discharge of the vacuum.
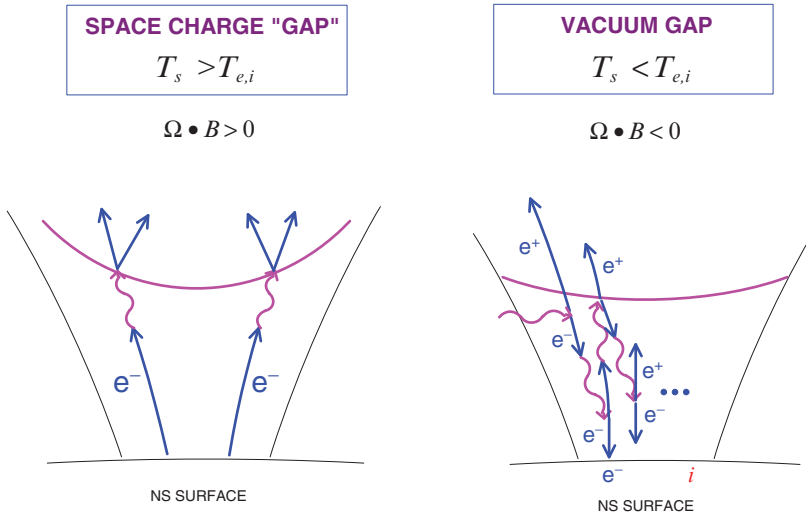

Fig. 19.1 Illustration of space-charge limited flow and vacuum gap accelerators above a pulsar polar cap. T_s is the neutron star surface temperature and $T_{i,e}$ are the ion or electron thermionic temperatures

The potential drop in the gap thus oscillates between $V_{vg} \sim \Omega B_0 (R\theta_{PC})^2/2$ and 0. In SCLF for $\Omega \cdot B (>,<)0$, an electron/positron accelerates upward from the surface until the radiated photons reach pair threshold, at which point the positrons/electrons from the pair decelerate, turn around, and accelerate downward toward the neutron star surface. The polarization of pairs above the pair formation front (PFF), discussed in more detail in Sect. 19.3, may short out the $E_\parallel$, halting any further acceleration at higher altitude. These accelerators can thus maintain a steady current of upwardly accelerating electrons, at $j_\parallel^- \simeq c\rho_{GJ}$, and a downward current of positrons, at $j_\parallel^+ \ll c\rho_{GJ}$, which heat the polar cap. The accelerator voltage is determined by the height of the PFF, which is again roughly comparable to the pair creation mean-free path. However, the stability of SCLF accelerators has not yet been verified through time-dependent models, and some simplified studies [46] have in fact shown that some oscillations in the pair creation rate could exist. This is certainly an issue that needs further investigation. Stability of vacuum gaps has also been studied by Gil et al. [25].

19.2.2 Death Lines

The pair cascades can be initiated either by curvature radiation (CR) [14] or by resonant or non-resonant inverse-Compton scattering (ICS) of stellar thermal X-rays by primary electrons [69]. Since for a given Lorentz factor the peak CR photon energy, $\varepsilon_\gamma = 3\lambda_C \gamma^3/2\rho_c$, where $\lambda_C \equiv h/mc$ is the electron Compton wavelength and ρ_c is the magnetic field radius of curvature, is much lower than the ICS peak energy, $\varepsilon_\gamma \sim \gamma$ in the extreme Klein-Nishina limit, pair production of CR photons requires a much higher particle Lorentz factor. The PFF for ICS therefore occurs at a lower altitude than the PFF for CR [33]. The PFF altitude is the sum of the acceleration length $\propto 1/E_\parallel$ and the pair attenuation length, which are both inverse functions of the magnetic field, and effectively of the pulsar age. If the PFF is larger than a stellar radius, then the magnetic field becomes too weak for pair creation to occur and a PFF does not exist. For SCLF accelerators, CR photons can produce pairs only in the case of young pulsars ($\tau \lesssim 10^7$ yr) and a few millisecond pulsars [34, 38]. One can define a 'death line' in $\dot{P} - P$ space, where $\dot{P}$ is the period derivative, shown in Fig. 19.2 below which pulsars cannot produce pairs from CR photons. Below the CR pair death line, pulsars can produce pairs only from ICS photons [35]. Below a lower, ICS pair death line, pulsars cannot produce any pairs and are expected to be radio quiet. In fact the predicted ICS death line falls close to the edge of the known radio pulsar population, as shown in Fig. 19.2 [36]. The few millisecond pulsars that lie below the ICS pair death line may be able to produce pairs through interaction of ICS photons with thermal X-ray photons from a hot polar cap [78].
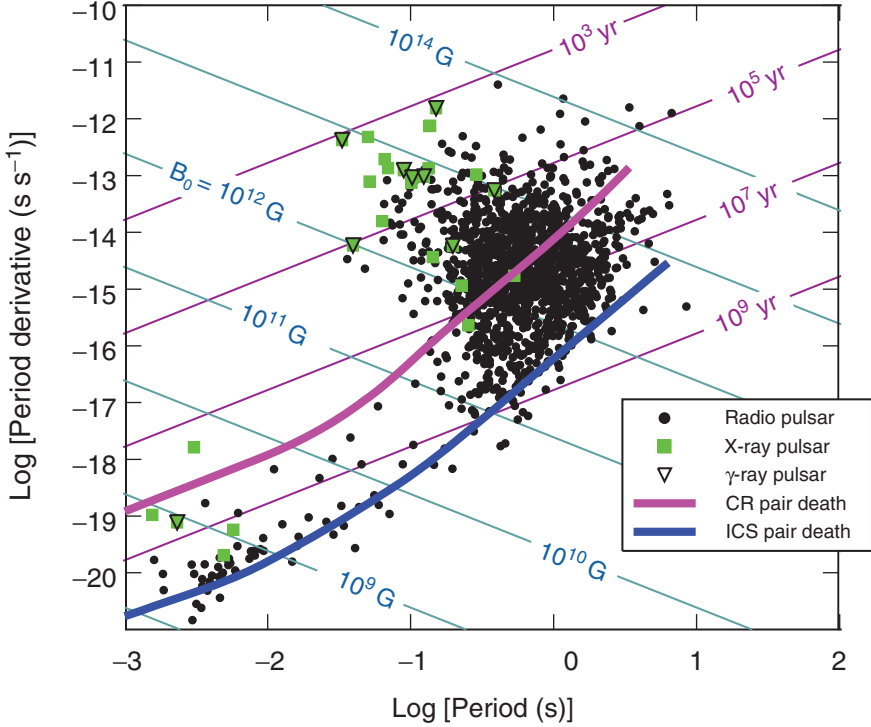
Fig. 19.2 Period derivative vs. period for radio and high-energy pulsars from the ATNF catalog, showing death lines [35] for production of electron-positron pairs through curvature radiation (CR) and inverse Compton scattering (ICS). The ICS pair death line was determined for a neutron star surface temperature of 10^6 K and a standard equation of state [8]

19.3 Electric Field Screening and Polar Cap Heating

In SCLF accelerators, the polarization of charge above the PFF acts both to screen the $E_\parallel$ and to produce heating of the polar cap by the downward flowing particles [4]. Figure 19.3 illustrates the dynamics of electric field screening. Primary electrons (e_p^-) accelerate upward from the stellar surface and produce pairs at different altitudes above the PFF. The positrons decelerate and turn around in a distance short compared to the PFF altitude and each reversing positron creates a small excess of negative charge. As more positrons are produced and decelerated, the space charge becomes more negative until the entire charge deficit $\delta\rho = (\rho - \rho_{GJ})$ that produced the $E_\parallel$ is accounted for. Since the charge deficit is small compared to the primary charge ($\delta\rho \ll \rho_{GJ}$), the screening length scale is a very small fraction of the PFF altitude. The flux of returning positrons, as a fraction of the primary flux, is approximately

$$f_+ \approx \frac{\rho_+}{\rho_{GJ}} = \left.\frac{\rho_{GJ} - \rho}{2\rho_{GJ}}\right|_{z_0} \approx \frac{3}{2}\frac{\kappa}{(1-\kappa)}z_0 \qquad (19.6)$$
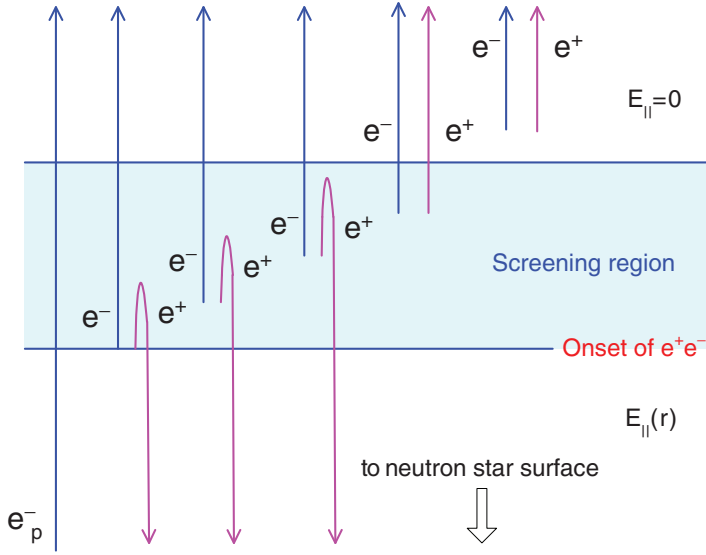
Fig. 19.3 Illustration of electric field screening in SCLF models. e_p^- represents the primary electron flux accelerating upward from the neutron star surface. e^+ and e^- represent electron-positron pairs created by the primary electron above the pair formation front

where z_0 is the PFF height above the stellar surface and κ is the general relativistic factor appearing in the SCLF electric field ((19.5)). The corresponding polar cap heating luminosity is

$$L_+^{\max} \approx f_+ \Phi(z_0) \dot{n}_{\mathrm{prim}} \tag{19.7}$$

where $\dot{n}_{\mathrm{prim}}$ is the primary particle flux and $\Phi(z_0)$ is the potential drop at z_0. The growth in the charge density above the CR PFF is very rapid since the CR peak energy $\varepsilon \propto \gamma^3$ increases rapidly with increasing electron Lorentz factor, γ. The CR initiated cascades have very high multiplicities and the screening of $E_\parallel$ takes place in a relatively short distance above the PFF [34]. The ICS initiated cascades on the other hand have much lower multiplicities since the ICS photon production rate decreases with increasing γ, as $\sim 1/\gamma$, for non-resonant scattering and first increases sharply, then decreases as $\sim 1/\gamma^2$ for resonant scattering. The screening above ICS PFFs takes place over a larger scale length, depending on the polar cap temperature and for a number of pulsars well below the CR pair death line, there is no screening [35]. Even when ICS screening is locally complete, an unscreened charge deficit can develop at higher altitudes since the charge density deficit $\delta\rho$ grows faster than the increase in pair density. In that case, an $E_\parallel$ reappears and acceleration continues. If a CR PFF forms at higher altitude, then screening occurs, otherwise unscreened acceleration continues to high altitude [56].

The CR pair heating luminosity is much higher than the ICS heating luminosity because the CR PFF occurs at higher altitude and a larger flux of positrons returns
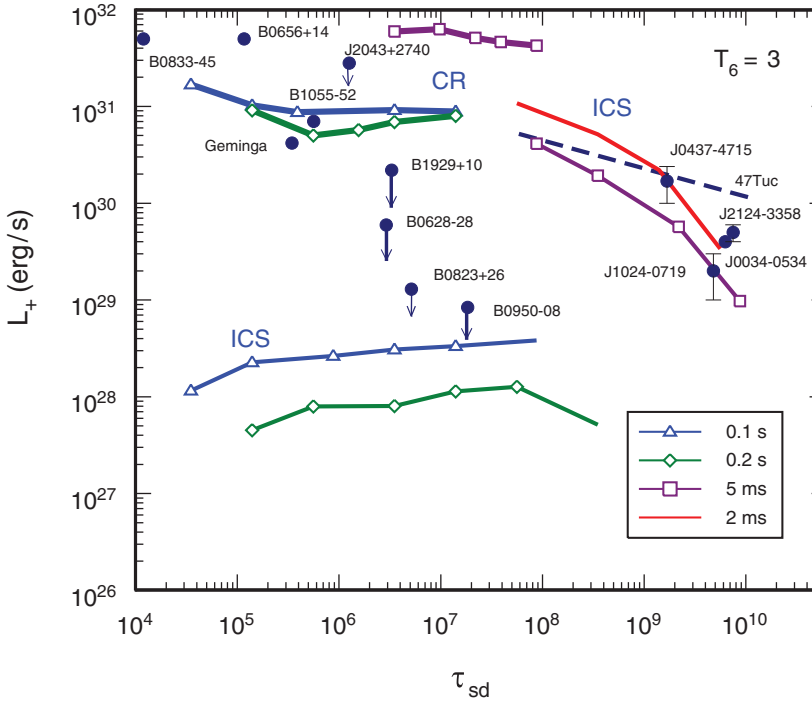
Fig. 19.4 Predicted polar cap heating luminosity, L_+, for SCLF model vs. spin down age [35], τ_{sd}, for different pulsar periods and an assumed polar cap surface temperature of 3×10^6 K. Thick curves are luminosities from curvature radiation (CR) pair heating and thin lines are luminosities from inverse Compton (ICS) pair heating. The solid circles show measured pulsar luminosities and upper limits of hot thermal components (see [42]). The dashed line is the fit of measured luminosity vs. age for the millisecond pulsars in the globular cluster 47 Tuc [10, 27]

through a higher voltage, bombarding the polar cap with higher energy. Figure 19.4 shows calculated heating luminosities from CR and ICS positrons as a function of pulsar characteristic age, $\tau_{sd} = P/2\dot{P}$, for several different periods and a PC surface temperature of $T = 3 \times 10^6$ K. The CR heating lines terminate on the high τ_{sd} side at the age corresponding to the CR pair death line, which is around $\tau_{sd} \sim 10^7$ yr for periods $P = 0.1, 0.2$ s and around $\tau_{sd} \sim 10^8$ yr for periods $P = 5$ ms. The CR heating luminosities are several orders of magnitude higher than the ICS heating luminosities, for normal pulsars. All the L_+ are higher for millisecond periods, because the PFFs occur at higher altitude and the gap voltage is larger. A sudden drop in L_+ is therefore predicted at the CR death line. Pulsed X-ray emission has now been detected from many middle-aged and older pulsars (cf. Chap. 6). Several thermal components are often seen, one having lower T and larger area, which may be full surface cooling, and another having a higher T and smaller area, which could be due to polar cap heating. The luminosity of the hot thermal components, which are shown in Fig. 19.4, may indicate that the heating luminosity drops suddenly around

$\tau_{sd} \sim 10^7$ yr or somewhat sooner. To within an order of magnitude, the observed luminosities of the hot thermal components agree with the predicted L_+, for both normal and millisecond pulsars.

Although the L_+ plotted in Fig. 19.4 were computed numerically, analytic expressions for L_+ provide a good estimate in the case of complete screening and upper limits in the case of incomplete screening. The heating from CR pair fronts predicts a surface X-ray luminosity of approximately [34]

$$L_+^{(CR)} \simeq 10^{31} \text{ erg s}^{-1} \begin{cases} 0.4\, P^{-6/7} \tau_6^{-1/7} & \text{if } P \lesssim 0.1\, B_{0,12}^{4/9}, \\ 1.0\, P^{-1/2} & \text{if } P \gtrsim 0.1\, B_{0,12}^{4/9}, \end{cases} \tag{19.8}$$

where $B_{0,12} = B_0/10^{12}$ G. The heating from ICS pair fronts predicts a surface X-ray luminosity of approximately [35]

$$L_+^{(IC)} \simeq 2.5 \times 10^{27} \text{ erg s}^{-1}\, P^{-3/2}. \tag{19.9}$$

Since nearly all millisecond pulsars produce only ICS pairs with incomplete screening, the above expression overestimates the predicted L_+ in these sources.

19.4 Slot Gap Accelerator

Due to the geometry of the field lines and the assumed boundary conditions of the accelerator, the altitude of the PFF varies with magnetic colatitude across the polar cap [5,33]. On field lines well inside the polar cap rim, $E_\parallel$ is relatively strong and the PFF is very near the neutron star surface. But at the polar cap rim, which is assumed to be a perfectly conducting boundary, $E_\parallel$ vanishes. Near this boundary, the electric field is decreasing and a larger distance is required for the electrons to accelerate to the Lorentz factor needed to radiate photons energetic enough to produce pairs. The PFF thus curves upward as the boundary is approached, forming a narrow slot gap (see Fig. 19.6) near the last open field line [5]. Since $E_\parallel$ is unscreened in the slot gap, particles continue to accelerate and radiate to high altitude along the last open field lines. The width of the slot gap is a function $\Lambda \equiv P B_{0,12}^{-4/7}$ of pulsar period and surface magnetic field [54], and can be expressed in magnetic colatitude as a fraction of the polar cap half-angle $\Delta \xi_{SG}$, where $\xi \equiv \theta/\theta_{PC}$

$$\Delta \xi_{SG} \simeq \begin{cases} 4\Lambda, & \Lambda < 0.075 \\ 0.3, & \Lambda > 0.075 \end{cases} \tag{19.10}$$

The particles can achieve very high Lorentz factors which at altitudes of several stellar radii are limited by curvature radiation losses, to $\gamma_{SG} \simeq 3 - 4 \times 10^7$ [55]. Since the slot gap is very narrow for young pulsars having short periods and high fields, the corresponding solid angle of the gap emission $\Omega_{SG} \propto \theta_{PC}^2 r \Delta \xi_{SG}$ is quite small. So even though only a small fraction of the polar cap flux is accelerated in the slot

gap, the radiated flux $\Phi_{SG} = L_{SG}/\Omega_{SG}d^2$ can be substantial. The total luminosity divided by solid angle from each pole is (from [54])

$$\frac{L_{SG}}{\Omega_{SG}} = \varepsilon_\gamma \left[0.123\cos^2\alpha + 0.51\,\theta_{PC}^2\sin^2\alpha\right] \text{erg s}^{-1}\,\text{sr}^{-1}$$

$$\times \begin{cases} 9\times10^{34}\,L_{sd,35}^{3/7}P_{0.1}^{5/7}, & B < 0.1\,B_{\text{cr}} \\ 2\times10^{34}\,L_{sd,35}^{4/7}P_{0.1}^{9/7}, & B > 0.1\,B_{\text{cr}} \end{cases} \qquad (19.11)$$

where $P_{0.1} \equiv P/0.1$ s, $L_{sd,35} \equiv L_{sd}/10^{35}\,\text{erg s}^{-1}$ is the spin down luminosity, $B_{\text{cr}} \equiv 4.4\times10^{13}$ G is the critical magnetic field strength and ε_γ is the efficiency of conversion of primary particle energy to high-energy emission.

For $\Lambda \gg 0.075$, which corresponds to pulsars below the CR pair death line (see Fig. 19.2), the slot gap disappears since the screening of $E_\parallel$ is no longer effective. These "pair-starved" pulsars may have local screening of $E_\parallel$ near the ICS PFF, but $E_\parallel \neq 0$ at higher altitude so that acceleration can occur over nearly all of the open field volume [56]. The particle Lorentz factors, as in the slot gap, will be limited by curvature-radiation reaction to $\gamma \sim 10^7$.

19.5 High-energy Radiation

19.5.1 Polar Cap and Slot Gap Cascades

As discussed in Sect. 19.2.2, pair cascades above the polar cap may be initiated by either ICS or CR. In the strong magnetic fields near the neutron star, the Compton scattering cross section has a resonance at the cyclotron energy, $\varepsilon_B \sim 12B_{12}$ keV, where its value is several orders of magnitude higher than the Thompson cross section. The thermal X-rays from the neutron star surface will be blue-shifted into the resonance in the rest frame of the accelerating primary electrons when $kT\gamma(1 - \beta\cos\theta) \simeq \varepsilon_B$, where θ is the angle between the photon propagation and the electron velocity (i.e. the magnetic field direction). Since the enhancement of the cross section at the resonance is so large, resonance scattering will dominate if the resonance condition is met [16, 74]. For typical pulsar fields and surface temperatures, electrons with $\gamma \sim 10^2 - 10^6$ will resonant scatter surface thermal X-rays [33, 79] to energies $\varepsilon \simeq \gamma B'mc^2$, where $B' \equiv B/B_{\text{cr}}$ is the magnetic field strength in units of the critical field strength, $B_{\text{cr}} = 4.4\times10^{13}$ G. X rays scattered by electrons with $\gamma \sim 10^5 - 10^6$ will produce pairs to form a PFF. Resonant scattering is the dominant mode of ICS pair production for pulsars having the highest fields [38], whereas pulsars with lower fields, that include the millisecond pulsars, produce ICS pairs through non-resonant scattering. For $\gamma \gtrsim 10^5$, the electrons will scatter non-resonantly in the Klein-Nishina limit, to energies $\varepsilon \simeq \gamma$. The ICS pair cascade multiplicities are $M_+^{ICS} \simeq N_+/N_p \sim 10^{-3} - 10$ (pairs per primary electron) [38], which is too low and produced at too low an altitude to completely shut off the acceleration.

When the primary electrons reach $\gamma \gtrsim (0.5 - 1) \times 10^7$, they produce CR photons that can produce pairs to form a PFF at height $0.02 - 0.1$ stellar radii. The CR pair cascade multiplicities reach as high as $M_+^{CR} \simeq 10^3 - 10^4$ [3, 38].

The pairs are produced in Landau states whose maximum principal quantum number is $n_{max} = 2\varepsilon'(\varepsilon' - 2)/B'$ [15], where $\varepsilon' = \varepsilon \sin\theta$ is the photon energy in the frame in which it propagates perpendicular to the local magnetic field. When the local field $B \lesssim 0.1 B_{cr}$, pairs will be created above threshold in highly excited Landau states and the excitation level is quite sensitive to field strength, $n_{max} \propto 1/B'^3$. The pairs will decay through emission of synchrotron/cyclotron photons, many of which will produce more pairs in excited states. A pair cascade can be sustained in such a way through several generations. The pairs can also produce ICS photons, through scattering surface thermal X-rays, which may produce pairs [77]. In high-field pulsars, where $B \gtrsim 0.1 B_{cr}$ near the neutron star surface, the pair creation attenuation coefficient is high enough for pair creation near threshold, so pairs are produced in very low Landau states. In this case, cascade pair multiplicities are lower since the number of cyclotron photons drop significantly [7]. Bound pair production [65] also becomes important for $B \gtrsim 0.1 B_{cr}$, which will further lower the pair multiplicity. When $B \gtrsim B_{cr}$, photon splitting dominates over pair production [31]. The screening of the electric field is also delayed by splitting and creation of bound pairs, effectively increasing the accelerating potential. The effect of bound pair creation on polar cap acceleration has been studied by Usov & Melrose [73].

Radiated spectra from CR-initiated [14] and ICS-initiated [69] cascades are very hard (roughly power laws with indices 1.5–2.0) [30] with sharp cutoffs due to magnetic pair production at energy [28, 31]

$$E_c \sim 2 \text{ GeV } P^{1/2} \left(\frac{r}{R}\right)^{1/2} \max\left\{0.1, B_{0,12}^{-1} \left(\frac{r}{R}\right)^3\right\} \tag{19.12}$$

where r is the emission radius and R is the neutron star radius. An approximate form for the polar cap pair cascade spectrum is given by

$$f(\varepsilon) = A\varepsilon^{-a} \exp\left[-C_{1\gamma}\exp\left(-\varepsilon_{esc}^{1\gamma}/\varepsilon\right)\right] \tag{19.13}$$

where a is the power-law index, $C_{1\gamma} = 0.2(\alpha/\lambdabar)(B'R^2/\rho)$ and $\lambdabar = \lambda_C/2\pi$ is the electron Compton wavelength. The polar cap cascade radiation produces a hollow cone of emission around the magnetic pole, with opening angle, $\theta_\gamma \simeq (3/2)(\Omega r/c)^{1/2}$, determined by the polar cap half-angle at the radius of emission r. The characteristics of emission from this type of polar cap model [17] has been successful in reproducing many features of γ-ray pulsars, including the wide double-peaked pulses observed from γ-ray pulsars like the Crab, Vela and Geminga, and the phase-revolved spectra. However, the polar cap opening angle is very small (a few degrees) unless the emission occurs more than a few stellar radii above the surface [19]. Since the pair cascades over most of the polar cap occur within several stellar radii of the stellar surface, the broad profiles which require beam opening angles of the order of the magnetic inclination angle α, cannot be produced unless the pulsar
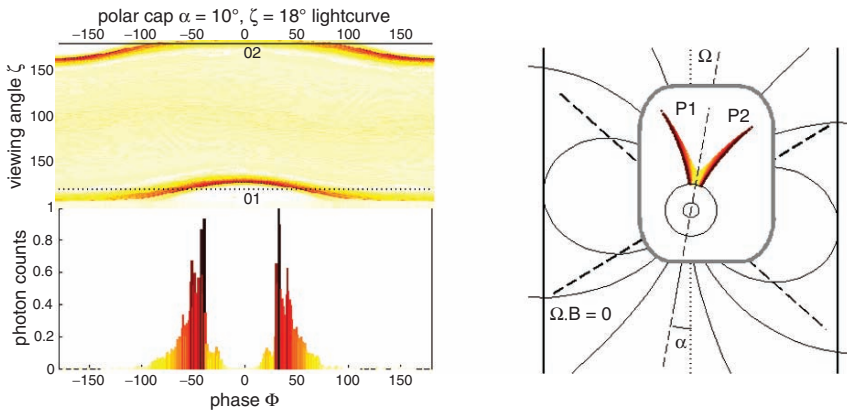
Fig. 19.5 Phase plot, sample lightcurve, and a sketch of the accelerator location for the polar cap model, for a typical inclination angle $\alpha = 10°$. The central zoom gives the gap extent relative to the star size. The dashed lines outline the null surface. The shading in the lightcurve and gap sketch is the same. The phase plot illustrates the change in lightcurve as seen by different observers and the aperture of the pulsed beams (from [26])

is nearly aligned. Daugherty & Harding [17] had to assume extended acceleration to 3 stellar radii and an artificial enhancement of primary particle flux near the polar cap rim in order to reproduce the Vela pulsar spectrum and pulse profile.

Muslimov & Harding [54] found that pair cascades on the inner edge of the slot gap occur at altitudes of 3–4 stellar radii and have higher multiplicities, $M_+ \sim 10^4 - 10^5$, than the polar cap cascades. These are the characteristics required by [17] to model γ-ray pulsars, so a combination of polar cap cascades near the stellar surface and slot gap cascades near the polar cap rim at higher altitude may be successful in explaining non-thermal radiation from some fraction of sources having small magnetic inclination α and viewing angles ζ. Figure 19.5 shows a plot of the total sky emission, phase Φ vs. viewing angle ζ relative to the rotation axis, for a slot gap cascade at inclination angle $\alpha = 10°$. In this model, the magnetic pole is at phase $0°$, midway between the two peaks in the profile, which would be the predicted phase peak of polar cap thermal emission.

19.5.2 Radiation from the High-altitude Slot Gap

The electrons that accelerate in the slot gap and generate pair cascades at low altitude continue to accelerate. They will radiate curvature, inverse Compton and synchrotron radiation at high altitudes. Initially, their Lorentz factors will be limited by curvature-radiation reaction, to

$$\gamma_{CRR} = \left(\frac{3}{2} \frac{E_{||} \rho_c^2}{e} \right)^{1/4} \sim 3 \times 10^7 \qquad (19.14)$$

and the peak energy of their CR spectrum will be $\varepsilon_{peak}^{CR} = 2\lambda_C \gamma_{CRR}^3 / \rho_c \approx 30 \text{GeV}$. As the electrons reach higher altitude, where the local magnetic field has dropped to $B \sim 10^6 - 10^8$ G, they may be able to resonantly absorb radio photons of energy $\varepsilon_{0,GHz}$ that are at the cyclotron resonance in their rest frame. The condition for resonant absorption is

$$\gamma_R = 3 \times 10^5 \frac{B_8}{\varepsilon_{0,GHz}(1 - \beta\mu_0)} \tag{19.15}$$

where $B_8 \equiv B/10^8$ G and μ_0 is the cosine of the angle between the radio photon and the electron momentum. The electrons are then excited to higher Landau states and radiate synchrotron emission. Blandford & Scharlemann [9] investigated this process for pulsars, concluding that it was not an important source of radiation. However, they assumed that the electrons would be excited to only low Landau states and based their estimate on the cyclotron emission rate. Decades later, Lyubarsky & Petrova [48] re-examined resonant cyclotron absorption of radio emission in pulsar magnetospheres and discovered that the rate of absorption is much higher than the rate of re-emission in low-lying Landau states, so the electrons will continue to be excited to high Landau states, and their pitch angles will increase until their momentum perpendicular to the magnetic field is relativistic. The emission is then synchrotron, not cyclotron, which proceeds at a much higher rate. Petrova [61] concluded that this process could be a significant source of radiation for young pulsars. It could also be significant for millisecond pulsars with high radio luminosities like PSR J0218+4232 ([37] and Sect. 19.5.4).

In the slot gap or along open field lines of pair-starved pulsars, electrons can experience both continuous acceleration and resonant cyclotron absorption. A steady-state may be reached between synchrotron radiation (SR) losses and absorption, with perpendicular momentum

$$\frac{p_\perp^{SRR}}{mc} \simeq 302 B_8^{-1} E_{\parallel,5}^{1/2} \tag{19.16}$$

which can indeed be relativistic. In this state, the Lorentz factor can remain locked at $\gamma_R \ll \gamma_{CRR}$ to the cyclotron resonance as the electron moves along the field with the field decreasing [37]. The synchrotron peak frequency decreases with increasing altitude, spreading the emission over a range of energies up to ~ 100 MeV, and the curvature radiation rate drops dramatically.

Non-resonant inverse Compton scattering of the radio emission by relativistic electrons in the slot gap is also possible. The scattering would be completely in the Thompson regime, and the spectrum would extend to a maximum energy of $\varepsilon_{\max} \sim \gamma_{CRR}^2 \varepsilon_{0,GHz} \sim$ a few GeV. This process might make a significant contribution to the total spectrum of the slot gap if the radio emission region is located at relatively high altitude (see Sect. 19.6.1).

19.5.3 Relativity, Geometry and Causties

The geometry of emission at high altitude is strongly influenced by special rela-
tivistic effects of aberration, time-of-flight and retardation of the magnetic field.
Aberration and time-of-flight produce phase shifts of comparable magnitudes $\Delta\Phi \sim -r/R_{LC}$ in radiation emitted at different altitudes r relative to the light cylinder
radius R_{LC}. Morini [53] first noted that the combined phase shifts from aberration
and time-of-flight, of photons radiated tangent to a magnetic dipole field from the
polar cap to the light cylinder, nearly cancel those due to field line curvature on
the trailing edge of the open-field region. Radiation along such trailing field lines
bunches in phase, forming a sharp emission peak or caustic in the phase plot or
profile (Fig. 19.6). On the leading side, these phase shifts add up to spread pho-
tons emitted at various altitudes over a large range of phases. The effect is most
pronounced for large α and emission between altitudes $r_{em} \sim 0.2 - 0.8 R_{LC}$. Sweep-
back of the magnetic dipole field due to retardation [18,75] affects photon emission
directions near the light cylinder, and also distorts the polar cap and open field vol-
ume [2, 20], even at the stellar surface. Most observer angles sweep across caustics
from both magnetic poles, resulting in a double peaked pulse profile where the peaks
generally have phase separation less than 180° [22]. Furthermore, emission occurs
at all phases in the profile. Such profiles are very similar to those of the bright γ-ray
pulsars, Crab and Vela. The predicted polarization characteristics of such a "two-
pole caustic" model can also explain the observed optical polarization of the Crab
pulsar [21].

Radiation from the slot gap has a geometry very similar to that of the "two-pole
caustic" model and thus displays caustics in the intensity phase plots as well as Crab-
like pulse profiles [55]. The high-altitude slot gap thus may be a viable model for
high-energy emission from young pulsars. However particle acceleration in the slot
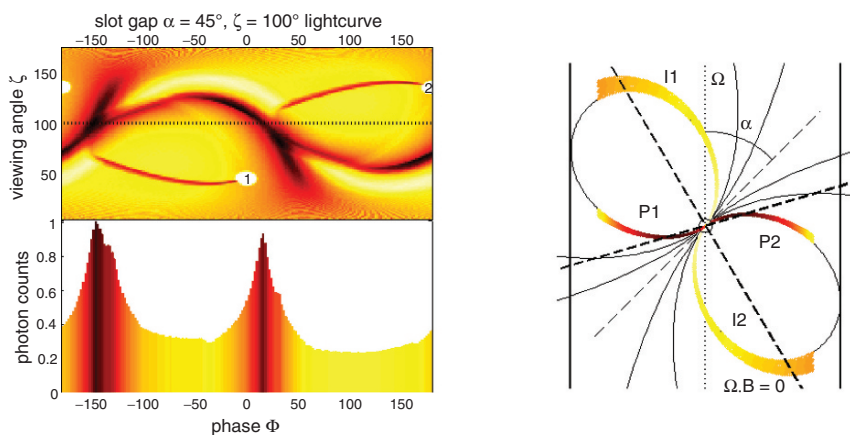

Fig. 19.6 Same as Fig. 19.5 for the slot gap model, for a typical inclination angle $\alpha = 45°$ (from
[26])

gap may not operate at all inclination angles. The low altitude $E_\parallel$, shown in (19.5), is a function of both α and ϕ. For large α and $\cos\phi < 1$ (field lines curving away from the rotation axis), the second term in (19.5) can become large and negative at large r, causing the $E_\parallel$ to reverse sign. This would cause a buildup of charge at that location, and would clearly be an unstable situation. The charge flow along those field lines might then be either time-dependent or non-existent. The solution for $E_\parallel$ at high-altitude in the slot gap [55] may moderate this effect somewhat, but for fast rotators and $\alpha \gtrsim 70°$ the $E_\parallel$ reverses sign at low altitude. The resolution to this problem is still forthcoming, but it is possible that steady current flow in the slot gap does not occur for all geometries.

19.5.4 Radiation from Millisecond Pulsars

There are more than 200 radio pulsars now known with periods between 1 and 30 ms. Many (around 30) have been detected as X-ray point sources, and seven of these have X-ray pulsations. Only the few millisecond pulsars (MSPs) that lie above or near the CR pair death line are expected to have slot gaps. These include B1821-24, B1957+20 and B1937+21, whose pulse profiles interestingly show caustic-like narrow, sharp peaks. The rest that lie below the CR death line are pair-starved and their SCLF $E_\parallel$ is unscreened. Particles on all open field lines will therefore accelerate to high-altitude with Lorentz factors limited by CR losses, as in the slot gap (19.14). The peak energy of the CR spectrum for MSPs is similarly high, $\varepsilon^{CR}_{peak} \approx 10\,\mathrm{GeV} B_8^{3/4} P_{ms}^{-5/4} \kappa_{0.15}^{3/4}$, where $P_{ms} = P/1ms$ and $B_8 = B/10^8$ G. But the very low magnetic fields of MSPs do not absorb the high energy part of the spectrum, so these sources may be visible up to energies of 50 GeV [11, 36, 49]. The CR will dominate for viewing angles near the magnetic poles because the emission comes primarily from low altitude, since the particle Lorentz factors decrease with increasing altitude. Additionally, as discussed in Sect. 19.5.2, synchrotron radiation from resonant absorption of radio emission may be important for MSPs having high radio luminosities. The synchrotron component will appear in the X-ray to γ-ray ($\lesssim 100\,\mathrm{MeV}$) region of the spectrum [37], and will be visible at a larger range of observer angles since the emission comes from high altitudes. Figure 19.7 shows a model spectrum for the millisecond pulsar PSR J0218+4232 based on a (1D) cyclotron resonant absorption model described above (see 19.5.2).

19.6 Pulsar Emission at Multi-wavelengths

Since rotation-powered pulsars shine over a broad spectrum from radio to high-energy γ-ray wavelengths, the multi-wavelength spectra and profiles can give important clues to the acceleration and emission geometry. Although there are some clear patterns of spectral behavior with pulsar age (cf. Chap. 6), the observed
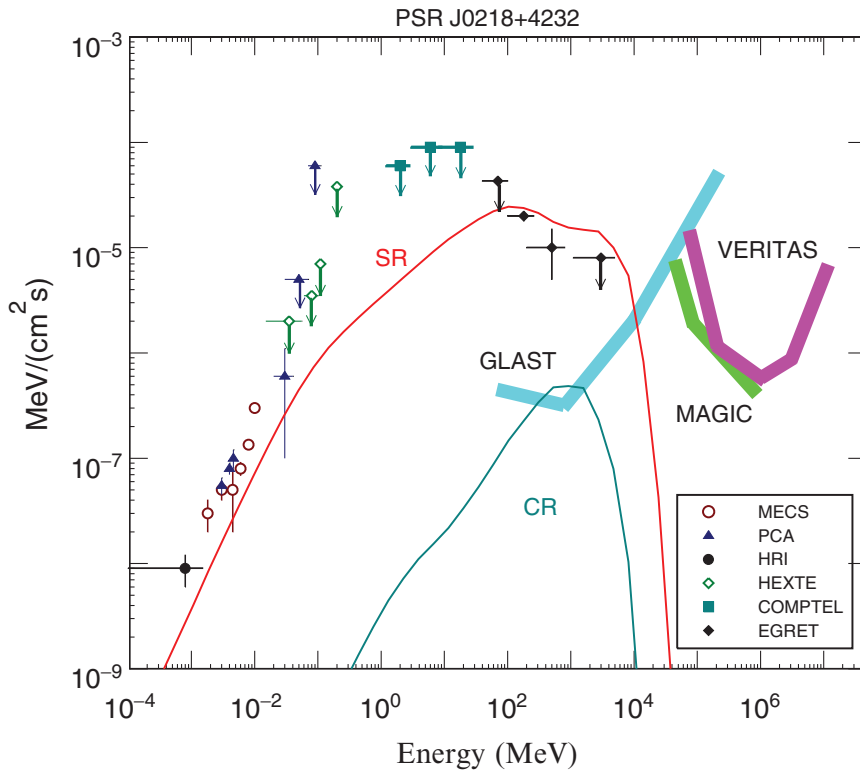
Fig. 19.7 Model spectrum for 2.3 ms PSR J0218+4232 (from [37]) showing components from synchrotron radiation (SR) and curvature radiation (CR) from unscreened acceleration of a single primary electron, from the NS surface to the light cylinder, along a field line defined by magnetic colatitude $\xi = 0.9$ in units of PC half angle, at inclination $\alpha = 50°$. Data points are from [45]

multi-wavelength lightcurves show a wide variety of characteristics that present many puzzles. As shown in Fig. 19.8, the lightcurves for the known γ-ray pulsars do not as a rule exhibit much phase correspondence between radio, X-ray and γ-ray peaks. The sole example is the Crab pulsar, where two peaks separated by $\sim$140° are in phase from radio to γ-ray energy. For the other pulsars, the radio peak usually leads the one or two γ peaks in phase and the soft X-ray peaks are broader and overlap the γ-ray peaks. Comparing X-ray and radio profiles of known rotation-powered X-ray pulsars, one sees that there is more multi-wavelength phase coherence for shorter periods ($P \lesssim 50$ ms), such as for PSR B0540-69 (50 ms), PSR J1617-5055 (69 ms) and the millisecond pulsars, PSR B1821-24, PSR B1937+21 and PSR J0218+4232. Such short-period and younger pulsars also tend to have pure power law X-ray spectra with no thermal components (cf. Chap. 6), indicating that their X-ray emission is primarily non-thermal radiation from accelerated particles. One possible picture is that pulsars with shorter periods accelerate particles mostly in the outer magnetosphere, in slot gaps or outer gaps. The high-energy
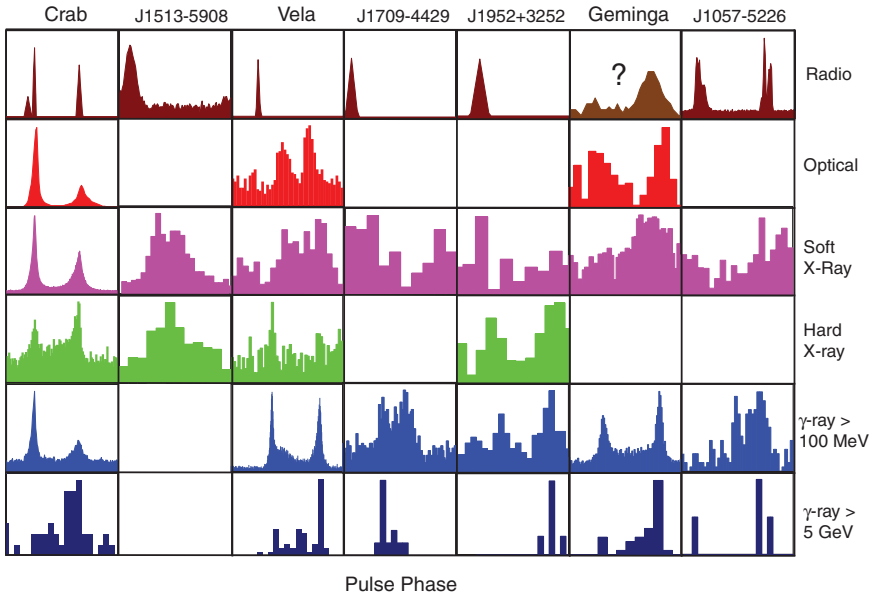
Fig. 19.8 Profiles of seven γ-ray pulsars in six energy bands, as in [70]

emission occurs at high altitudes that are large fractions of their light cylinder radii, $R_{LC} = 5 \times 10^9 P^{-1}$ cm, which are also smaller. Their emission geometry is therefore expected to be different from that of longer period pulsars, whose high-energy emission occurs closer to the neutron star surface and at altitudes that are very small fractions of R_{LC}.

19.6.1 Radio Emission Geometry

Because the mechanism responsible for the radio beams is not understood, and more importantly because the radiation is coherent, it has not been possible to describe this emission using a physical model. The emission has therefore been described using empirical models, developed over the years through detailed study of pulse morphology and polarization characteristics. The emission is also highly polarized, and displays changes in polarization position angle across the profile that often matches the swing expected for a sweep across the open field lines near the magnetic poles in the Rotating Vector Model [62]. Empirical models (e.g. [63]) characterize pulsar radio emission as having a core beam centered on the magnetic axis and one or more hollow cone beams outside of the core. The average-pulse profile widths and component separations are measured to be decreasing functions of radio frequency [66]. This is consistent with a hollow cone beam centered on the magnetic pole, emitted at an altitude that decreases with increasing frequency

(radius-to-frequency mapping). From such profile width measurements, and assuming that the edges of the pulse are near the last open field line, Kijak & Gil [43] find an emission radius of

$$r_{\text{radio}} \approx .01\, R_{LC} \left(\frac{\dot{P}}{10^{-15}\,\text{s s}^{-1}} \right)^{0.07} P^{-0.7} \nu_{GHz}^{-0.26} \qquad (19.17)$$

where $\dot{P}$ is the period derivative. This result predicts that for pulsars with $P \lesssim 0.1$ s the emission radius $r_{\text{radio}} \gtrsim 0.05 - 0.1\, R_{LC}$. Such a picture is independently supported by polarization studies [40] of pulsars younger than 75 kyr. They concluded that the emission of these pulsars was from a single wide cone beam, that core emission was weak or absent, and that the height of the cone emission is between 1% and 10% of the light cylinder radius.

19.6.2 The Global Picture

As discussed in Sect. 19.5.3, emission along the last open field lines at altitudes $r_{\text{em}} \sim 0.2 - 0.8\, R_{LC}$ will form caustics, producing sharp peaks in the pulse profiles. According to (19.17), the radio cone emission altitude for pulsars with periods $P \lesssim 30 - 50$ ms, depending on their $\dot{P}$, will fall in the range of caustic formation. If the radio conal emission is radiated over an extended range of altitude (i.e. a few tenths of R_{LC}) then radio caustic peaks would appear in phase with high-energy caustic peaks. Such a model would explain the multi-wavelength phase coherence of the profiles of fast pulsars like the Crab and millisecond pulsars, PSR B1821-24 and PSR B1937+21. The conal emission of slower pulsars would fall below the altitude range of caustic formation and the radio conal peak(s) or core emission would lead the high-energy caustic peaks, as seen in most of the multi-wavelength profiles of Fig. 19.8. In these cases, a single radio peak leading double γ-ray peaks is most likely to be the edge of a cone beam, since it is unlikely that a viewing angle crosses the narrow core beam as well as both caustics. For example, the observer viewing angle illustrated in Fig. 19.6 would cross the outer edge of pole 2 at a phase of 180°. Due to the radius-to-frequency mapping of the cone emission, this picture would predict that the measured width of the radio beam would be smaller at higher frequency since the emission is originating at lower altitude, whereas the core emission width would not be expected to vary with frequency.

Aside from the geometry of the emission at different wavelengths, that is directly relevant to observational characteristics of pulsars, there is the more fundamental question of how the microphysics of acceleration and pair cascades fit into the studies of the pulsar magnetosphere. The magnetosphere models [13, 68] make the assumption of ideal MHD (no parallel electric fields) in order to derive the global structure of the magnetic field and currents that are solutions to the so-called pulsar equation [51] that describes a spinning neutron star with a dipole field. A notable feature of these models is the formation of a neutral sheet in the equatorial plane of the spin axis which may provide a source of the return current that flows back

to the neutron star along the last open field line. The derived currents in such models do not match the currents that have been assumed in either polar cap or outer gap accelerator models. Yet the microphysical acceleration models are needed to describe the physics of the pair creation and to check the consistency of the assumption of ideal MHD conditions over most of the magnetosphere. At present, it is not clear whether the global models can be adjusted to match the boundary conditions of the acceleration models [71] or the whether the acceleration models can produce the required cascade multiplicity with compatible boundary conditions. In the end, self-consistency between global models and acceleration models may require time-dependence or spatial-dependence of the current flow.

19.7 Open Questions

Although much of the theoretical picture presented in this article depends on a set of undisputed fundamentals, such as, that rotation-powered pulsars are neutron stars with large-scale dipole magnetic fields that are directly measurable from their period derivatives, to within uncertainties in the equation of state. But the picture also involves a number of underlying assumptions that are less well confirmed or agreed upon. The most important of these for particle acceleration are the boundary conditions on the charge flow. Both polar cap and outer gap acceleration models assume that the boundary between the open and closed field line region is a perfect conductor. This implicitly assumes that there is some microphysical screening at this boundary by charges in the closed-field region, although this process has not been modeled or simulated. The boundary condition on the electric field and potential at the neutron star depends on the binding energy of charge in the surface layers. Calculations of the cohesive force for a solid lattice in magnetic fields up to about 10^{13} G indicate that charges will not be bound in the surface at temperatures above ~ 0.5 MK, so that most pulsars have surfaces hot enough to allow SCLF accelerators to operate. However, a number of pulsars have magnetic fields above 10^{13} G, where surface conditions have not been adequately explored. It is possible that the neutron star surface may be in a liquid rather than solid state in very high magnetic fields [32, 41] or that charges may be bound by much stronger forces. In this case, high-field pulsars could have vacuum instead of SCLF accelerators.

Models often also assume that the neutron star is a dipole field in calculating the accelerating electric potential and field. This assumption could be faulty at low altitude if there exist higher multipole fields near the neutron star surface, and is certainly invalid at very high altitude where there are distortions of the field due to retardation [20] and current flow [57]. The $E_{\parallel}$ in the high altitude slot gap [55] is only approximate and needs to be calculated using field line distortions. It is possible that the distorted field lines, having less curvature than a dipole, will have the effect of removing the sign reversals present in the approximate solutions. There are also expected to be cross field particle motions at high altitude that will modify solutions of the electric field.

The possible connection of pair cascades to radio emission morphology is an intriguing question that needs further investigation. For example, are the pairs from the near-surface polar cap and high-altitude slot gap cascades responsible for the core and cone beams? Do pairs produced in the outer gaps produce any radio emission? Whether polar caps and slot gaps can exist on the same field lines or in the same pulsar magnetosphere is also not known.

Although some of these questions require more theoretical work, it is hoped that many answers will come from observations with future detectors. The Large Area Telescope (LAT) on the Gamma-ray Large Area Space Telescope (GLAST), due to launch in 2008, will have unprecedented sensitivity and energy resolution for gamma-rays in the range of 30 MeV to 300 GeV. GLAST is therefore expected to provide major advances in the understanding of high-energy emission from rotation-powered pulsars (cf. Chap. 23 and [29]), including an increase in the number of detected radio-loud and radio-quiet gamma-ray pulsars, and millisecond pulsars, giving much better statistics for elucidating population characteristics, measurement of the high-energy spectrum and the shape of spectral cutoffs and determining pulse profiles for a variety of pulsars of different ages. Further, measurement of phase-resolved spectra and energy dependent pulse profiles of the brighter pulsars should allow detailed tests of magnetospheric particle acceleration and radiation mechanisms. Third-generation ground-based Air Cherenkov detectors, such as H.E.S.S. [58] in Namibia, MAGIC [47] in the Canary Islands and VERITAS [39] in the US, have begun operation. They are sensitive to γ-rays in the range 50 GeV to 50 TeV and are putting important constraints on pulsar spectra and emission mechanisms [1]. Further into the future are planned X-ray telescopes, such as IXO, and X-ray polarimeters, such as AXP, POGO and ACT. Polarimeters in particular will be extremely important in verifying model predictions for different pulsar emission geometries through phase-resolved measurements of position angle and polarization percent (cf. Chap. 22 by Weisskopf et al.).

References

1. Aharonian, F. et al. A & A, 466, 543 (2007)
2. Arendt, P. N. & Eilek, J. A. (astro-ph/98011257) (1998)
3. Arendt, P. N. & Eilek, J. A. ApJ, 581, 451 (2002)
4. Arons, J. ApJ, 248, 1099 (1981)
5. Arons, J. ApJ, 266, 215 (1983)
6. Arons, J. & Scharlemann, E. T. ApJ, 231, 854 (1979)
7. Baring, M. G. & Harding, A. K. ApJ, 547, 929 (2001)
8. Baym, G., Pethick, C. & Sutherland, P. ApJ, 170, 299 (1971)
9. Blandford, R. D. & Scharlemann, E. T. MNRAS, 174, 59 (1976)
10. Bogdanov, S. et al. ApJ, 646, 1104 (2006)
11. Bulik, T., Rudak, B. & Dyks, J. MNRAS, 317, 97 (2000)
12. Camilo, F. Young Neutron Stars and Their Environments, IAU Symposium 218, Ed. F. Camilo and B. M. Gaensler. San Francisco, CA: Astronomical Society of the Pacific, p. 97 (2004)
13. Contopoulos, I., Kazanas, D. & Fendt, C. ApJ, 511, 351 (1999)
14. Daugherty, J. K. & Harding, A. K. ApJ, 252, 337 (1982)

15. Daugherty, J. K. & Harding, A. K. ApJ, 273, 761 (1983)
16. Daugherty, J. K. & Harding, A. K. ApJ, 336, 861 (1989)
17. Daugherty, J. K. & Harding, A. K. ApJ, 458, 278 (1996)
18. Deutsch, A. Annales d'Astrophysique, 18, 1 (1955)
19. Dyks, J. & Rudak, B. A & A, 393, 511 (2002)
20. Dyks, J. & Harding, A. K. ApJ, 614, 869 (2004)
21. Dyks, J., Harding, A. K. & B. Rudak, ApJ, 606, 1125 (2004)
22. Dyks, J. & B. Rudak, ApJ, 598, 1201 (2003)
23. Edwards, R.T., Bailes, M., van Straten, W. & Britton, M.C. MNRAS, 326, 358 (2001)
24. Goldreich, P. & Julian, W. H. ApJ, 157, 869 (1969)
25. Gil, J., Melikidze, G. & Zhang, B. A & A, 457, 5 (2006)
26. Grenier, I. A. & Harding, A. K. In Proceedings of Einstein Centenary Conference, Paris 2005, AIP Conference Proceedings, 861, 630–637 (2006)
27. Grindlay et al. ApJ, 581, 470 (2002)
28. Harding, A. K. In High Energy Gamma-Ray Astronomy, Ed. F. A. Aharonian & H. J. Volk, AIP Conference Series Vol. 558 (AIP: New York), 115 (2001)
29. Harding, A. K. In proceedings of First GLAST Symposium, ed. S. Ritz, P.F. Michelson & C. Meegan (AIP), in press (2007)
30. Harding, A. K. & Daugherty, J. K. Adv. Space Res., 21, 251 (1998)
31. Harding, A. K., Baring, M. G. & Gonthier, P. L. ApJ, 476, 246 (1997)
32. Harding, A. K. & Lai, D. Rep. Prog. Phys., 69, 2631 (2006)
33. Harding, A. K. & Muslimov, A. G. ApJ, 508, 328 (1998)
34. Harding, A. K. & Muslimov, A. G. ApJ, 556, 987 (2001)
35. Harding, A. K. & Muslimov, A. G. ApJ, 568, 862 (2002)
36. Harding, A. K., Muslimov, A. & Zhang, B. ApJ, 576, 366 (2002)
37. Harding, A. K., Usov, V. V. & Muslimov, A. G. ApJ, 622, 531 (2005)
38. Hibschman, J. A. & Arons, J. ApJ 554, 624 (2001)
39. Holder, J. In Proceedings of Science with the New Generation of High Energy Gamma-Ray Experiments. The Variable Gamma-Ray Sources: Their Identifications and Counterparts. Eds. M. M. Massai, N. Omodei, G. Spandre. ISBN-13 978-981-270-964-6. World d Scientific Publishing, p. 69 (2007)
40. Johnston, S. & Weisberg, J. M. MNRAS, 368, 1856 (2006)
41. Jones, M. D. & Ceperley, D. M. PhRvL, 76, 4572 (1996)
42. Kaspi, V. M., Roberts, M. S. E. & Harding, A. K. In Compact Stellar X-ray Sources, Ed. W.H.G. Lewin & M. van der Klis. Cambridge: Cambridge University Press, pp. 279–339 (2006)
43. Kijak, J. & Gil, J. A & A 397, 969 (2003)
44. Krause-Polstorff, J. & Michel, F. C. MNRAS, 213, 43P (1985)
45. Kuiper, L., Hermsen, W. & Stappers, B. 2003, Pulsars, AXPs and SGRs observed with BeppoSAX and Other Observatories, Proceedings of the International Workshop held in Marsala, Edited by G. Cusumano, E. Massaro, T. Mineo. Roma, Italy: Aracne Editrice, July 2003, ISBN 88-7999-514-6, pp. 31–36, astro-ph/0306622.
46. Levinson, A., Melrose, D., Judge A. & Luo Q. ApJ, 631, 456 (2005)
47. Lorenz, E. High Energy Gamma-Ray Astronomy: 2nd International Symposium, Eds. F. A. Aharonian, H. J. Vlk, and D. Horns. AIP Conference Proceedings, Volume 745. New York: American Institute of Physics, pp. 622–627 (2005)
48. Lyubarskii, Y. E. & Petrova, S. A. A&A, 337, 433 (1998)
49. Luo, Q., Shibata, S. & Melrose, D. B. MNRAS, 318, 943 (2000)
50. Manchester, R. N. et al. MNRAS, 328, 17 (2001)
51. Michel, F. C. ApJ, 180, 207 (1973)
52. Mignani, R. P., DeLuca, A. & Caraveo, P. A. In "Young Neutron Stars and Their Environments" (IAU Symposium 218, ASP Conference Proceedings), Ed. F. Camilo and B. M. Gaensler. San Francisco: ASP, p. 39 (2004)
53. Morini, M. MNRAS, 303, 495 (1983)
54. Muslimov, A. G. & Harding, A. K. ApJ, 588, 430 (2003)

55. Muslimov, A. G. & Harding, A. K. ApJ, 606, 1143 (2004a)
56. Muslimov, A. G. & Harding, A. K. ApJ, 617, 471 (2004b)
57. Muslimov, A. G. & Harding, A. K. ApJ, 630, 454 (2005)
58. Hinton, J. A. et al. New Astron. Rev., 48, 331 (2004)
59. Muslimov, A. G. & Tsygan, A. I. MNRAS, 255, 61 (1992)
60. Petri, J., Heyvaerts, J. & Bonazzola, S. A & A, 384, 414 (2002)
61. Petrova, S. A. A&A, 408, 1057 (2003)
62. Radhakrishnan, V. & Cooke, D. J. ApL, 3, 225 (1969)
63. Rankin, J. M. ApJ, 405, 285 (1993)
64. Ruderman, M. A. & Sutherland, P. G. ApJ, 196, 51 (1975)
65. Shabad, A. E. & Usov, V. V. Nature, 295, 215 (1982)
66. Sieber, W., Reinecke, R. & Wielebinski, R. Astron. Astrophys., 38, 169 (1975)
67. Spitkovsky, A. Young Neutron Stars and Their Environments, IAU Symposium 218, Ed. F.
    Camilo and B. M. Gaensler. San Francisco, CA: Astronomical Society of the Pacific, p. 357
    (2004)
68. Spitkovsky, A. ApJ, 648, L51 (2006)
69. Sturner, S. J., Dermer, C. D. & Michel, F. C. ApJ, 445, 736 (1995)
70. Thompson D. J. In Cosmic Gamma-Ray Sources, Ed. K. S. Cheng & G. E. Romero. New
    York: Kluwer, ApSS, 304, 149 (2004)
71. Timokhin, A. MNRAS, 36, 1055 (2006)
72. Usov, V. V. & Melrose, D. B. Aust. J. Phys., 48, 571 (1995)
73. Usov, V. V. & Melrose, D. B. ApJ, 464, 306 (1996)
74. Xia, X. Y., Qiao, G. J., Wu, X. J. & Hou, Y. Q. Astr. Ap., 152, 93 (1985)
75. Yadigaroglu, I. A., Ph.D. Thesis, Stanford University (1997)
76. Zhang, B. & Harding, A. K. ApJ, 535, L51 (2000)
77. Zhang, B. & Harding, A. K. ApJ, 532, 1150 (2000)
78. Zhang, B. & Qiao, G. J. A & A, 338, 62 (1998)
79. Zhang, B. & Qiao, G. J. A & A, 310, 135 (1996)